Ionics (2022) 28:295–305
https://doi.org/10.1007/s11581-021-04312-6

ORIGINAL PAPER

An aqueous zinc pyrovanadate nanowire cathode doped by nitrogen-doped carbon from PANI calcination for capacity and stability enhancement

Feifei Wang[1] · Qiguan Wang[1] · Shibo Dong[1] · Sumin Wang[1]

Received: 18 April 2021 / Revised: 25 August 2021 / Accepted: 4 October 2021 / Published online: 11 October 2021

Abstract

Environmentally friendly aqueous zinc-ion batteries (AZIBs) have unique advantages, safer and less flammable than lithium-ion battery and lead acid batteries. The crucial issue is the poor mechanical stability and low electronic conductivity, resulting in insufficient rate capability and shortened cycle life. In this paper, by thermal-decomposition of polyaniline (PANI) at high temperature, the nitrogen-doped carbon (NDC) is formed and doped in zinc pyrovanadate (ZVO) nanowires. According to theoretical simulation, after doped by NDC the band gap of ZVO is greatly decreased and the structure stability is increased. As a result, the ZVO/NDC as cathode demonstrates large capacity of 295 mAh g^{-1} at the 0.1 A g^{-1} current density and a high-rate capability. In addition, ZVO/NDC nanowires also show a fairly large mass energy density of 132.8 mWh kg^{-1} and a volumetric energy density of 39.84 mWh L^{-1}, along with a high long-term stability (91% retention after 5000 charge–discharge cycling at 1.0 A g^{-1}). The present work certifies the proof-of-concept that exploiting nitrogen-rich carbon-doped electrodes for AZIBs in the future electronics.

Keywords Aqueous zinc-ion batteries · Nitrogen-doped carbon · ZVO · Long-term stability

Introduction

Lithium-ion battery (LIB) has been regarded as the most promising technology in various energy storage applications. However, flammable electrolyte, limited lithium reserves, and high cost restrict the wide application of current commercial LIBs [1–3]. These issues have motivated the design of the rechargeable water-based batteries, with simple processing, high ionic conductivity, and kind safety [4–6]. Among the new developed aqueous batteries, the rechargeable aqueous zinc-ion batteries (AZIBs) are important promising ones due to their low redox potential (− 0.76 V vs SHE), high theoretical capacity (819 mAh g^{-1} or 5851 mAh cm^{-3}), and great earth abundance of elemental zinc [7–10].

✉ Qiguan Wang
qiguanwang@163.com

✉ Sumin Wang
suminwang@163.com

[1] Shaanxi Key Laboratory of Photoelectric Functional Materials and Devices, School of Materials and Chemical Engineering, Xi'an Technological University, Xi'an 710021, People's Republic of China

So far, many materials have been employed as the cathode for AZIBs [11–13], among which layer-type vanadium-based compounds [14, 15] possessing open framework structure show high energy density, owing to the multiple-valence oxidation states of vanadium [16]. In spite of those advantages, vanadium-containing materials still show limitation of fast capacity decay as a result of their relatively poor electronic conductivity. Additionally, the repetitive reversible Zn^{2+} intercalation/deintercalation also causes their dissolution and self-aggregation [17, 18], which increase the contact resistance and impede the electrochemical reaction, resulting in a fall in the energy density and high-rate ability. Therefore, improvements in both the conductivity and structure stability have been the basement for vanadium-based compounds used in rechargeable applications.

To overcome the above-mentioned drawbacks, several approaches have been attempted, for example, directly growing vanadium-containing active compounds on superior conductive current collects [19–21]. Commonly used method is to coat conductive materials on the vanadium-based cathode. By this approach, the prepared PEDOT/V_2O_5 hybrid electrode illustrated a specific capacity as high as 232 mAh g^{-1} at the 20 A g^{-1} current density, as well as excellent cycle

life (97% retention after 600 cycles at 1 A g^{-1} and 89% after 1000 cycles) [22], due to the promoted transport kinetics of zinc ions.

As is known, there present lots of defects in crystalline materials during their growth [23], which significantly influence the stability of the crystalline layered structure, especially in the volumetric swelling and shrinking along with ions intercalation/deintercalation. In our recent work, N-doped carbons (NDC) were fabricated by polyaniline carbonization at high temperature, which was employed to have atomic doping on $NiCo_2O_4$ nanostructures [24], showing attractive electrochemical applications. Here, we demonstrate a zinc pyrovanadate nanowire doped by nitrogen-doped carbon (ZVO/NDC) from calcination of zinc pyrovanadate/polyaniline (ZVO/PANI), as illustrated in Fig. 1. The great interaction and charge transfer occurred between nitrogen in NDC and Zn^{2+} in ZVO, which enhances the electron transportation and the structural stability of the system. As a result, the functional AZIB with NDC-doped ZVO cathode displays larger specific capacity and better long-term cycling stability in comparison with the pristine ZVO.

Experimental section

ZVO synthesis

First, 1.5 mmol $Zn(NO_3)_2{\cdot}2H_2O$ was dissolved in 20 mL of deionized (DI) water. Then, 1.0 mmol of NH_4VO_3 powder was dissolved in another beak containing 20 mL deionized water and stirred at 80 °C for 10 min to form a clear yellow solution. Afterwards, the NH_4VO_3 solution is dripped into the zinc nitrate solution and stirred for 5 min. The obtained solution is then transferred to a tetrafluoroethene reactor at 180 °C and held for 6 h. After cooling, the synthesized product is collected and rinsed with alcohol and DI water, and then dried under vacuum at 50 °C for 48 h.

PANI preparation

3.2 mmol aniline was dissolved in 10 mL 1.0 M HCl, in which 10 mL hydrogen chloride solution (1.0 M) containing 0.8 mmol of ammonium persulfate was quickly poured and stirred continuously under ice bath for 1 h. The product was filtered, washed with ethyl alcohol and deionized water, and dried at 60 °C for 6 h.

ZVO/NDC composite

0.05 mL aniline was dissolved in 10 mL HCl (1 M), and 216 mg ZVO was added to the solution. Then, 17.2 mg of ammonium persulfate was dissolved in 10 mL 1.0 M HCl and then added into the above solution. After stirred at 0 °C for 1 h, the mix solution was filtered, washed with alcohol and deionized water. The ZVO/PANI product was obtained after dried at 60 °C for 6 h. To get the ZVO/NDC composite, the ZVO/PANI was calcinated at 800 °C for 6 h in a tube furnace in N_2 atmosphere. Pure NDC was obtained by calcining PANI in N_2 atmosphere at high temperature.

Cell construction

Firstly, polyvinylidene fluoride (PVDF), Super-P, and the ZVO/NDC samples were mixed according to the mass ratio of 1:2:7 in N-methylpyrrolidone (NMP) until viscous slurry was obtained, and coated on the steel mesh. After dried at 100 °C in argon atmosphere, the electrode is assembled in the order of positive electrode, polyethylene-polypropylene membrane, and negative electrode, which were placed in a CR2016 coin-type battery case and sealed under pressure. The galvanostatic charge–discharge (GCD) test was

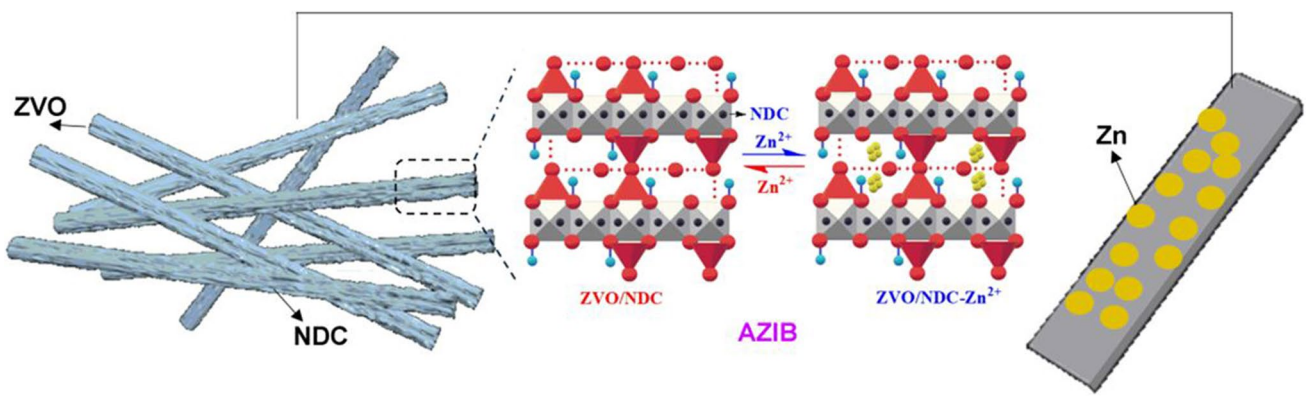

Fig. 1 Schematic illustration of ZVO/NDC nanowires and the intercalation/deintercalation of Zn^{2+}

performed on a CT3008W Neware battery test machine. The 1 M $ZnSO_4$ aqueous solution is used as electrolyte.

Instruments and equipment

Scanning electron microscope (SEM) images were performed on an S4800 instrument. Fourier transform infrared (FT-IR) spectra were detected on a Nicolet Magna-IR 750 spectrometer by using the KBr disk method. The ZVO/NDC powders were studied by JEM-2010 (JEOL, Japan) high-resolution transmission electron microscopy (HRTEM). The X-ray diffraction (XRD) data were measured from a Shimadzu XRD-6000 X-ray diffractometer, using the Cu Kα line with wavelength of 0.15416 nm as a radiation source. X-ray photoelectron spectra (XPS) were obtained by using a PHI 5400 XPS machine, calibrated with the C 1 s peak at 284.5 eV for sp^2 hybridized carbons. The electrochemical experiments were carried out employing a CHI660 workstation.

Electrochemical characterizations

The electrochemical measurements were performed on a conventional three-electrode system, employing a Pt wire as the counter electrode. The ZVO, ZVO/PANI, and ZVO/NDC were loaded on a glass carbon electrode (ø = 4 mm) and used as the working electrode. The loaded weight for every sample is 2.0 mg. To investigate the interfacial charge-transfer resistance of different working electrodes, electrochemical impendence spectroscopy (EIS) measurements were conducted in the frequency range of 10^5–10^{-1} Hz in the KOH solution (0.1 M) with an ac perturbation of 0.01 V.

Results and discussion

Firstly, the synthesis of ZVO nanofibers was completed. PANI was grown on the nanofibers in situ, and PANI wrapped the ZVO nanofibers tightly. Then ZVO/PANI was calcinated at high temperature to form nitrogen-doped carbon wrapped on ZVO, forming ZVO/NDC. In order to understand the morphological transformation and the change of structure during the synthesis process, the representative SEM and TEM images were acquired and demonstrated in Fig. 2. As can be seen from Fig. 2a and d, ZVO exhibits a uniform ultralong nanowire structure and many pores formed by the nanowire stacking. After in situ polymerization of aniline, the diameter of ZVO nanowire seems thickened as discerned from Fig. 2b and e, because of coating by PANI powder (see the arrows in Fig. 2b and e). As seen from Fig. 2c and f, the ZVO nanowire surface changed coarser after calcination at high temperature, mainly because PANI was decomposed to form N-doped carbon nanoparticles on ZVO surface, denoted by the arrows in Fig. 2c and f. This is helpful to improve the adsorption and transfer of electrolyte ions on ZVO. From the surface EDS mapping of ZVO shown in Fig. S1, the ZVO nanowires are composed of uniformly distributed Zn, V, and oxygen elements. After calcination of ZVO/PANI (Fig. S2), the resulting ZVO/NDC shows C and N, besides Zn, V, and O elements. This showed that the nitrogen-rich carbon decomposed from PANI was successfully doped in ZVO/NDC.

Figure 3a displays the XRD pattern of PANI, ZVO, and ZVO/NDC. The samples illustrated clear diffraction peaks that could be instructed well to pure phase of $Zn_3V_3O_8$ (JCPDS, No. 031–1477). From the XRD pattern of ZVO and

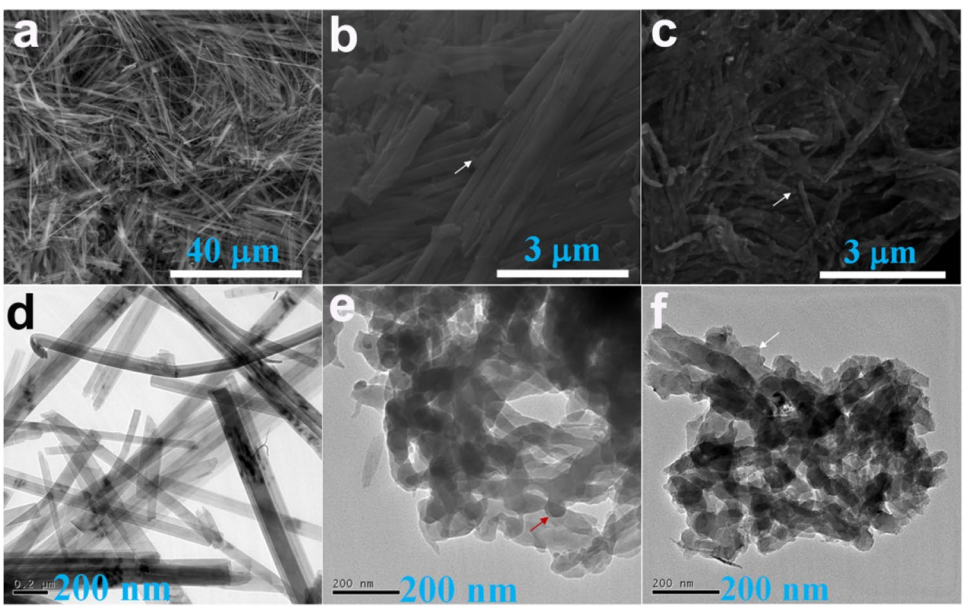

Fig. 2 SEM images of ZVO (**a**), ZVO/PANI (**b**), and ZVO/NDC (**c**). TEM images of ZVO (**d**), ZVO/PANI (**e**), and ZVO/NDC (**f**)

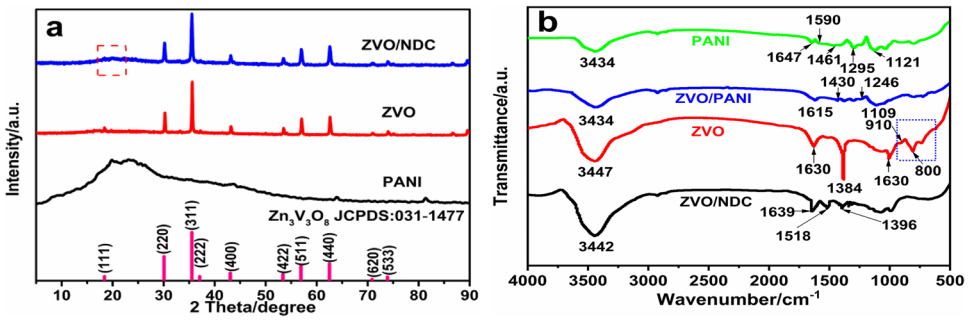

Fig. 3 XRD spectra (**a**) of PANI, ZVO, and ZVO/NDC. FT-IR spectra (**b**) of PANI, ZVO, ZVO/PANI, and ZVO/NDC

ZVO/NDC, characteristic peaks can be seen at 2θ = 18.4°, 30.1°, 35.5°, 37.1°, 43.1°, 53.4°, 56.9°, 62.5°, 70.8°, and 73.9°, corresponding to the crystal faces of (111), (220), (311), (222), (400), (422), (511), (440), (620), and (533), respectively, according to the JCPDS: No. 031–1477 [25]. After surface coating by NDC (Fig. 3a), the main features of ZVO were nearly unchanged. No characteristic peaks were observed for other impurities, indicating the high purity of the samples. This indicates the anchoring of NDC on ZVO cannot change the lattice property of ZVO. Moreover, there is a (002) diffraction peak of carbon at about 2θ = 20°, which can be attributed to the existence of a small amount of carbon in the material. The main reason is that PANI is calcined to form nitrogen-doped carbon wrapped on ZVO.

The FT-IR spectra of PANI, ZVO, ZVO/PANI, and ZVO/NDC were shown in Fig. 3b. The FT-IR spectrum of PANI illustrates that the N–H stretching vibration band is located at 3434 cm^{-1}, and the characteristic peaks at 1590 cm^{-1} and 1461 cm^{-1} are corresponded to stretching vibration of benzene and quinone rings in PANI [26]. The characteristic peak located at 1295 cm^{-1} is caused by the stretching vibration of C–N on the benzene ring. In addition, the band located at 1647 cm^{-1} is assigned to the C = N stretching vibration of the early formed phenazine units mingled with PANI products. The peak at 1121 cm^{-1} is assigned to the bending vibration of C–H in benzene of PANI. From the FT-IR spectrum of ZVO, it can be seen that characteristic peaks at 3447 cm^{-1} and 1630 cm^{-1} attributing to the symmetric and bending vibration of H–O–H bond in H_2O molecule are observed. The band at 1006 cm^{-1} is attributed to the symmetric vibration of V–O–Zn, and the bands located at 910 cm^{-1} and 800 cm^{-1} are corresponded to the asymmetric V–O–Zn and V–O–V vibration, respectively [27]. The intensive band located at 1384 cm^{-1} is resulted from the O–H stretching in the crystal frame.

However, for the ZVO/PANI, the characteristic bands attributed to C = N (1647 cm^{-1}), quinone and benzene ring (1461 cm^{-1}), and C–N (1295 cm^{-1}) stretching vibration in pure PANI are red-shifted to 1615 cm^{-1}, 1430 cm^{-1}, and 1246 cm^{-1}, respectively. This is because there occurs strong interactions between PANI and ZVO, which weakened the strength of C = N, quinone and benzene ring, and C–N bonds. Moreover, the peaks located at 1121 cm^{-1} corresponded to C–H bending vibration in benzene of PANI are also red-shifted to 1109 cm^{-1} in ZVO/PANI. Upon calcination, the spectrum of ZVO/NDC shows that two peaks at 1518 cm^{-1} and 1396 cm^{-1} are observed, attributing to the C = C stretching vibrations and C–N skeleton vibrations, together with the disappearance of features for quinone and benzene ring in PANI. Besides the wide features of ZVO ranged from 1000 to 500 cm^{-1}, the peak at 1639 cm^{-1} corresponds to the C = C stretching vibrations. Above results showed that PANI was decomposed and restructured, leading to nitrogen-doped carbons at high temperature.

Figure 4 shows the HRTEM images of ZVO and ZVO/NDC. The TEM images shown in Fig. 4a indicate the interior structure of the constituent ZVO microspheres, which is consistent with the SEM images. Meanwhile, the high-resolution transmission electron microscopy (HRTEM) characterized the detail structure of ZVO. The lattice fringes of ZVO can be seen clearly at very high magnification with a measured interplanar distance value of d = 0.240 nm (Fig. 4b), which corresponds to the (222) crystal planes of ZVO. It can also be seen from Fig. 4c that the ZVO exhibits specific monocrystalline structure from the periodic diffraction patterns. Figure 4d shows that the nanowire structure of ZVO maintained after calcination at high temperature. As seen from Fig. 4e and f, both regular diffraction spots and circular shapes appear in the HRTEM image of ZVO/NDC, meaning combination of both monocrystalline and polycrystalline nature. From Fig. 4f, the (111) and (220) planes are found, corresponding to the ZVO and the graphitic structures from calcination of polyaniline, respectively.

Figure 5 shows the chemical composition and valence states in ZVO, NDC, and ZVO/NDC detected by X-ray photoelectron spectroscopy (XPS). As seen from the wide scan XPS spectra of ZVO and ZVO/NDC (Fig. 5a), the C 1 s and N 1 s XPS signals are observed in ZVO/NDC besides the V 2p, O 1 s, and Zn 2p features compared with ZVO, due to the presence of carbon and nitrogen by calcination of PANI. The characteristic N 1 s feature of NDC can be deconvoluted into two peaks, as given in Fig. 5b. The peak located at 398 eV is attributed to the feature of pyridinic N (–N =), and the peak at 400.6 eV is owing to the feature of graphitic N (–NH–)

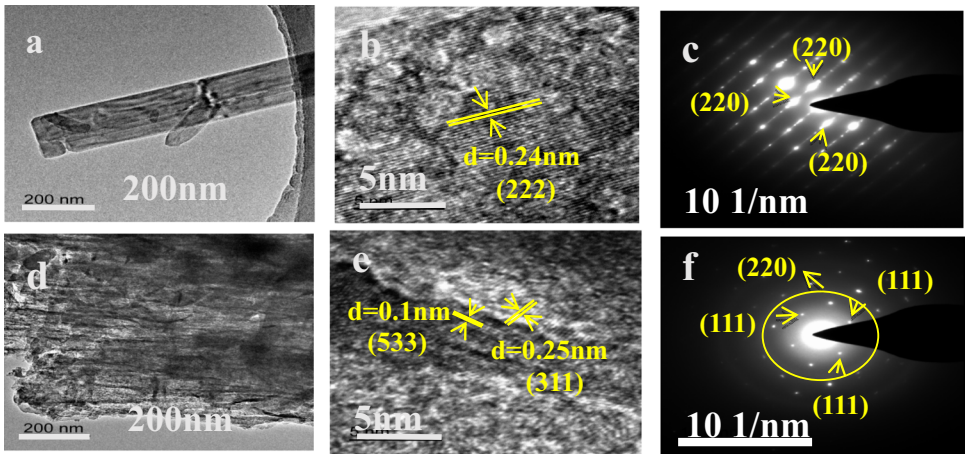

Fig. 4 HRTEM images of ZVO (**a**–**c**) and ZVO/NDC (**d**–**f**)

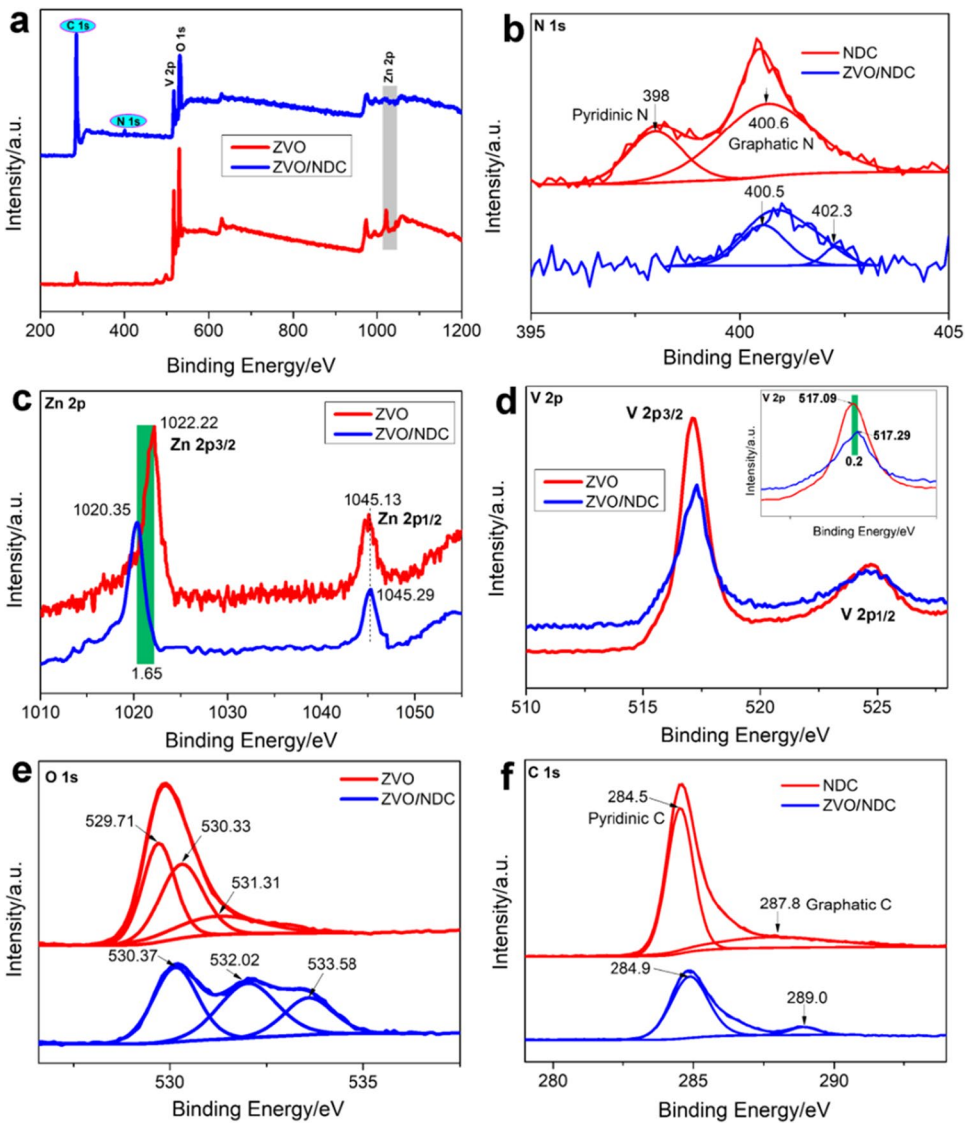

Fig. 5 Wide scan XPS spectra of ZVO and ZVO/NDC (**a**), and the deconvoluted N 1 s spectrum of NDC and ZVO/NDC (**b**), Zn 2p (**c**), V 2p (**d**), O 1 s (**e**) spectrum of NDC and ZVO/NDC, and C 1 s spectrum of NDC and ZVO/NDC (**f**). Inset in **d** shows the band gap of V 2p3/2 between ZVO and ZVO/NDC

[28]. In comparison with the corresponding deconvoluted N 1 s peaks of NDC, the N 1 s peaks in ZVO/NDC (400.5 eV and 402.3 eV in Fig. 5b) significantly shifted positively. The reason is possibly the charge transfer from nitrogen to zinc in the process of NDC doping on ZVO. It can be seen from the negative shift (about 1.65 eV) of Zn 2p3/2 signal [29] in ZVO/NDC compared with ZVO (Fig. 5c). Also, slight positive shift of V 2p3/2 [30] (0.2 eV, see inset in Fig. 5d) occurred in ZVO/NDC compared with ZVO due to the crystal structural distortion of ZVO after doped by NDC. Accompanied by the charge transfer in the doping process, the sharp positive shift of O 1 s and C 1 s features in ZVO/NDC is found compared with ZVO (Fig. 5e) and NDC (Fig. 5f), respectively.

Figure 6 illustrates the CV data of ZVO, ZVO/PANI, and ZVO/NDC in 1.0 M $ZnSO_4$ solution. As seen from Fig. 6a, the presence of two redox peaks at 1.12/0.61 V and 0.43/0.17 V can be assigned to the reversible Zn^{2+} (de)intercalation [31–34]. In addition, the CV peak intensity increases with the scanning rate increased from 10 to 50 mV s^{-1}. Composited with PANI, the resulting ZVO/PANI showed the similar redox peaks at 0.97/0.62 V and 0.24/0.31 V. After calcination, the formed NDC enhanced the oxidation–reduction of ZVO, there observes sharp redox peaks at 0.72/0.55 V and 0.42/0.17 V for ZVO/NDC in Fig. 6c. It can be seen from the figure that the decrease of the insertion and detachment potential makes it easier to carry out the insertion and detachment. The decrease of the peak gap makes the electron transmission ability enhanced, and the charge and discharge have reversible changes, which is conducive to improving the stability. Additionally, the peak gap between each redox reaction for ZVO/NDC decreased compared with that for ZVO, indication of the improved electron transportation of ZVO composited with NDC. Moreover, with the scan rate increase to 50 mV s^{-1}, a new oxidation peak at 1.18 V is observed, which may have relation with the doping of NDC on ZVO. In addition, the ZVO/NDC has the largest current density at the same scan rate in comparison with ZVO and ZVO/PANI, as illustrated from Fig. 6d.

Figure 7a–c shows cyclic voltammetry tests of ZVO, ZVO/PANI, and ZVO/NDC in 1.0 M $ZnSO_4$ solution with scan rates at 20, 40, 60, 80, and 100 mV s^{-1}, respectively. It can be found that ZVO/NDC shows the symmetrical quadrangular curves compared with ZVO and ZVO/PANI, indicating the better charge–discharge behavior. From Fig. 7d, ZVO, ZVO/PANI, and ZVO/NDC possess the electric double layer capacitance corresponding to 0.095675 mF cm^{-2}, 2.07 mF cm^{-2}, and 3.81 mF cm^{-2} respectively [35, 36]. Due to the NDC-doped ZVO, the ZVO/NDC still maintains a rectangular characteristic within a specific scanning range rate range, indicating that it has good conductivity.

Inset in Fig. 8A displays the Mott-Schottky plots of ZVO and ZVO/NDC. Both the ZVO and ZVO/NDC exhibit a negative slope, indicating the property of a p-type semiconductor [37,38]. As compared to ZVO, ZVO/NDC has a much lower slope, which corresponds to an increase of carrier density [39]. The enhanced carrier concentration explained the conductivity improvement of ZVO by composition with NDC, which also guarantees the structural stability of ZVO/NDC in charging/discharging. Figure 8B shows the impedance of ZVO, ZVO/PANI, and ZVO/NDC in 1 M $ZnSO_4$

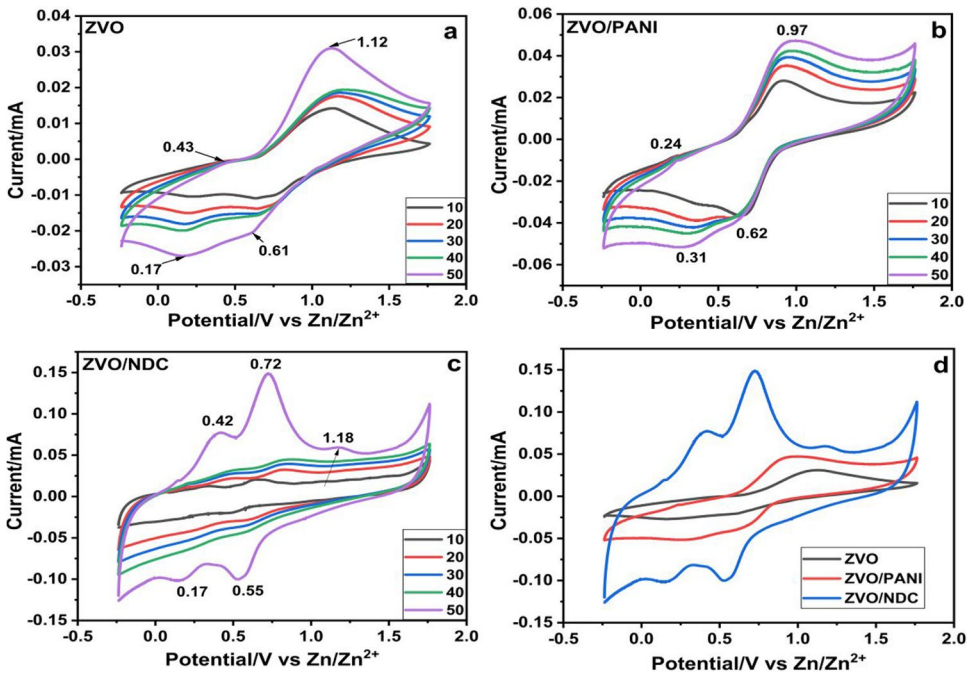

Fig. 6 CV curves of ZVO (**a**), ZVO/PANI (**b**), and ZVO/NDC (**c**). CV comparison (**d**) between ZVO, ZVO/PANI, and ZVO/NDC at 50 mV s^{-1}

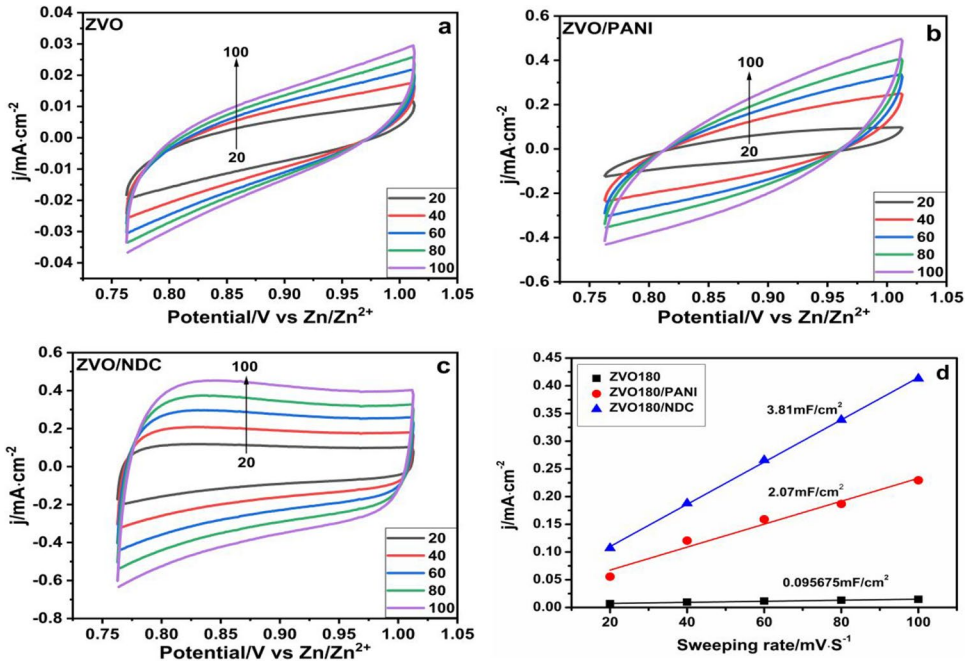

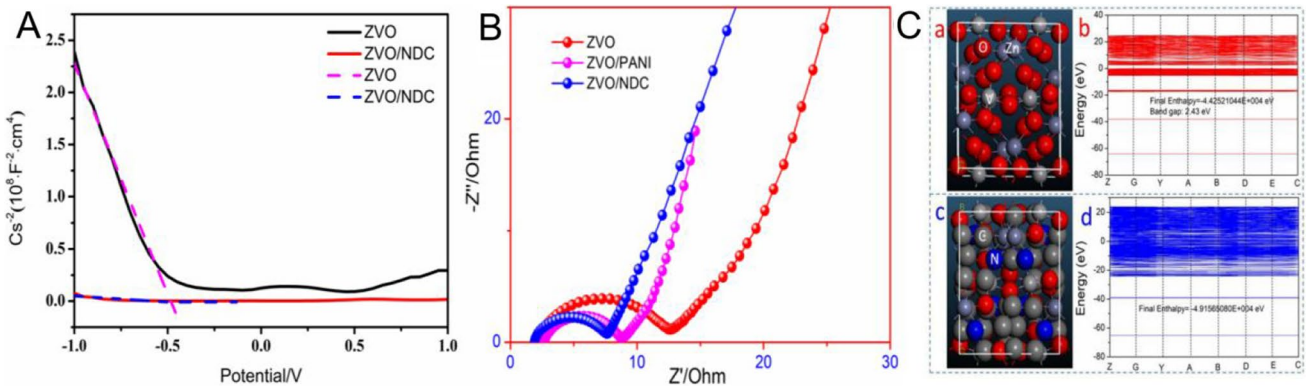

Fig. 7 CV curves of ZVO (**a**), ZVO/PANI (**b**), and ZVO/NDC (**c**) in 1 M $ZnSO_4$ solution. Fit curves of CV (**d**) for ZVO, ZVO/PANI, and ZVO/NDC

Fig. 8 Mott-Schottky plots of ZVO and ZVO/NDC (**A**), impedance diagrams of ZVO, ZVO/PANI, and ZVO/NDC (**B**), the geometry optimized crystal structure of ZVO (**a**) and ZVO/NDC (**c**), the calculated energy band for ZVO (**b**) and ZVO/NDC (**d**) (**C**)

solution, which illustrated similar EIS patterns consisting of a semicircle in the high-frequency region and a line in the low-frequency region. It can be seen that the radius of the semicircle in EIS spectrum for ZVO/NDC is lowest, which represents the smallest charge-transfer resistance and the largest ionic diffusion rate. The band structure feature of ZVO and ZVO/NDC is simulated on the grounds of density functional theory (DFT). The energy bands of ZVO have been calculated as observed in Fig. 8C. With one graphitic N unit of NDC composited in the ZVO (c of Fig. 8C), the number of ZVO bands increases (d of Fig. 8C) compared with ZVO sample (b of Fig. 8C), mainly due to the lattice distortion caused upon doping by NDC. In addition, the ZVO sample (a of Fig. 8C) gives the band gap with energy of 2.43 eV (b of Fig. 8C), while it greatly decreased to 0 eV for ZVO/NDC (d of Fig. 8C). This shows that ZVO/NDC can be used as a good conductor. Meanwhile, discerned from Fig. 8C, the final enthalpy of ZVO is lowered from − 44,252.1044 to about − 49,156.5080 eV, indicating that the structure stability of ZVO is enhanced by NDC doping. Above theoretical analysis shows that both the structural stability and the electrical conductivity of ZVO are improved after doped by NDC, explanation that the ZVO/NDC sample possesses low EIS resistance and excellent GCD cycling performances.

Additionally, an ex situ XRD measurement is carried out to determine the charge storage mechanism of ZVO/NDC. As depicted in Fig. 9a, all diffraction peaks of ZVO/NDC maintained during the charge/discharge process, which suggest the intrinsic structure of ZVO/NDC unable to be affected by the ion insertion/extraction. Notably, it can be

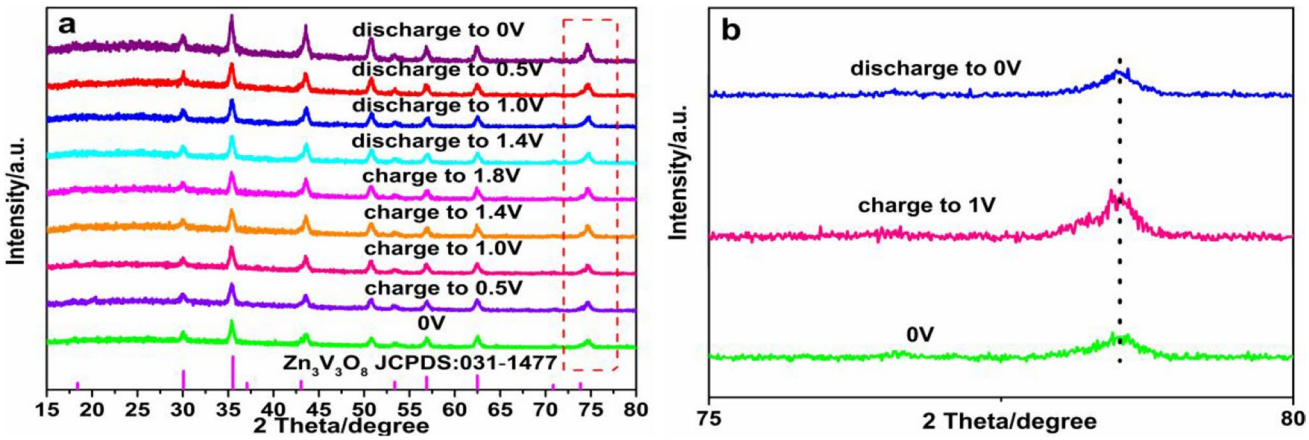

Fig. 9 The XRD variation of ZVO/NDC at different charging/discharging voltage (**a**) and the XRD variation near 2θ = 73.9° (**b**)

found that the peak position with diffraction angle at 73.9°, corresponded to crystal plane (533), shifted visibly during the charge/discharge processes. From Fig. 9b, the XRD peak at 73.9° shifted to the lower diffraction angle during charging until to 1.0 V, because the insertion of zinc ions expanded the lattice spacing. When discharged to 0 V with ion extraction, the peaks related to crystal plane (533) near 73.9° returned to the original position, implying the good reversibility and stability of the ZVO/NDC structure.

Figure 10a–c displays the CVs of ZVO, ZVO/PANI, and ZVO/NDC in different voltage windows in 1.0 M $ZnSO_4$. It can be seen that no polarization occurred for all the electrodes in 0–1.8 V from the unchanged shape of CV curves during variation of voltage windows. Figure 10d–f shows the galvanostatic charging and discharging of ZVO-based electrodes at different current densities. The ZVO/NDC electrode (Fig. 10f) has the longest discharging time compared with ZVO (Fig. 10d) and ZVO/PANI (Fig. 10e). In addition, as the current density increases, the discharging time becomes shorter and the capacity decreases for the three kinds of electrodes. As seen from Fig. 10g, the GCD test of NDC was performed on a CT3008W Neware battery test machine. The capacity of NDC at the current density 0.1 A g^{-1} is 189.8 mAh g^{-1}. Discerned from Fig. 10h, the capacity of ZVO and ZVO/PANI at the current density 0.1 A g^{-1} is 113 mAh g^{-1} and 160 mAh g^{-1}, respectively, and decreased to 17.5 mAh g^{-1} and 29 mAh g^{-1} at 2.0 A g^{-1}. However, for ZVO/NDC electrode, the capacity at current density 0.1 A g^{-1} reaches 295 mAh g^{-1}, and only decreased to 195 mAh g^{-1} when the current density was increased to 2.0 A g^{-1}. That is, ZVO/NDC shows a high-rate capability. The stack mass energy density of ZVO/NDC electrode is calculated as high as 132.8 mWh kg^{-1} at 295 mAh g^{-1}. It is noted that the capacity of ZVO/NDC is much higher that of the reported ultralong porous zinc pyrovanadate framework, which delivers capacities of 213 mAh g^{-1} at current density 50 mA g^{-1} [14]. In addition, compared with ZVO and ZVO/PANI (Fig. 10h), the charging and discharging stability of ZVO/NDC is seriously improved, indicating that the introduction of NDC enhances the conductivity and facilitates the electron transfer. Moreover, during long-term cycling under 1.0 A g^{-1}, the ZVO/NDC (Fig. 10i) gives the lowest capacity decay (9%) than ZVO (39%) and ZVO/PANI (22%) after 5000 cycles, showing potential applications in the energy-storage devices. Figure 8B displays the impedance of ZVO, ZVO/PANI, and ZVO/NDC, which illustrated similar EIS patterns consisting of a semicircle and a line in the high- and low-frequency region, respectively. It is found that the diameter of the semicircle in EIS curve for ZVO/NDC is lowest, representing the smallest charge-transfer resistance and the largest ionic diffusion rate. In order to calculate the mass energy density (E_g) and volumetric energy (E_V), the following Eqs. (1) and (2) were used [37].

$$E_g = \frac{C_m V^2}{2 \times 3.6} \ (\text{Wh kg}^{-1}) \tag{1}$$

$$E_V = E_g \times \text{ density of electrode (Wh L}^{-1}) \tag{2}$$

where C_m (F g^{-1}) represents the gravimetric capacitance and V equals the potential window (V). E_g (Wh kg^{-1}) represents the mass energy density and E_V (Wh L^{-1}) stands for the volumetric energy, respectively. Meanwhile, when the mass energy density is 132.8 mWh kg^{-1}, the volumetric energy density of ZVO/NDC is 39.84 mWh L^{-1}.

Conclusions

A nitrogen-doped carbon (NDC) is introduced into the open framework in zinc pyrovanadate (ZVO) by polyaniline (PANI) decomposition employing calcination method,

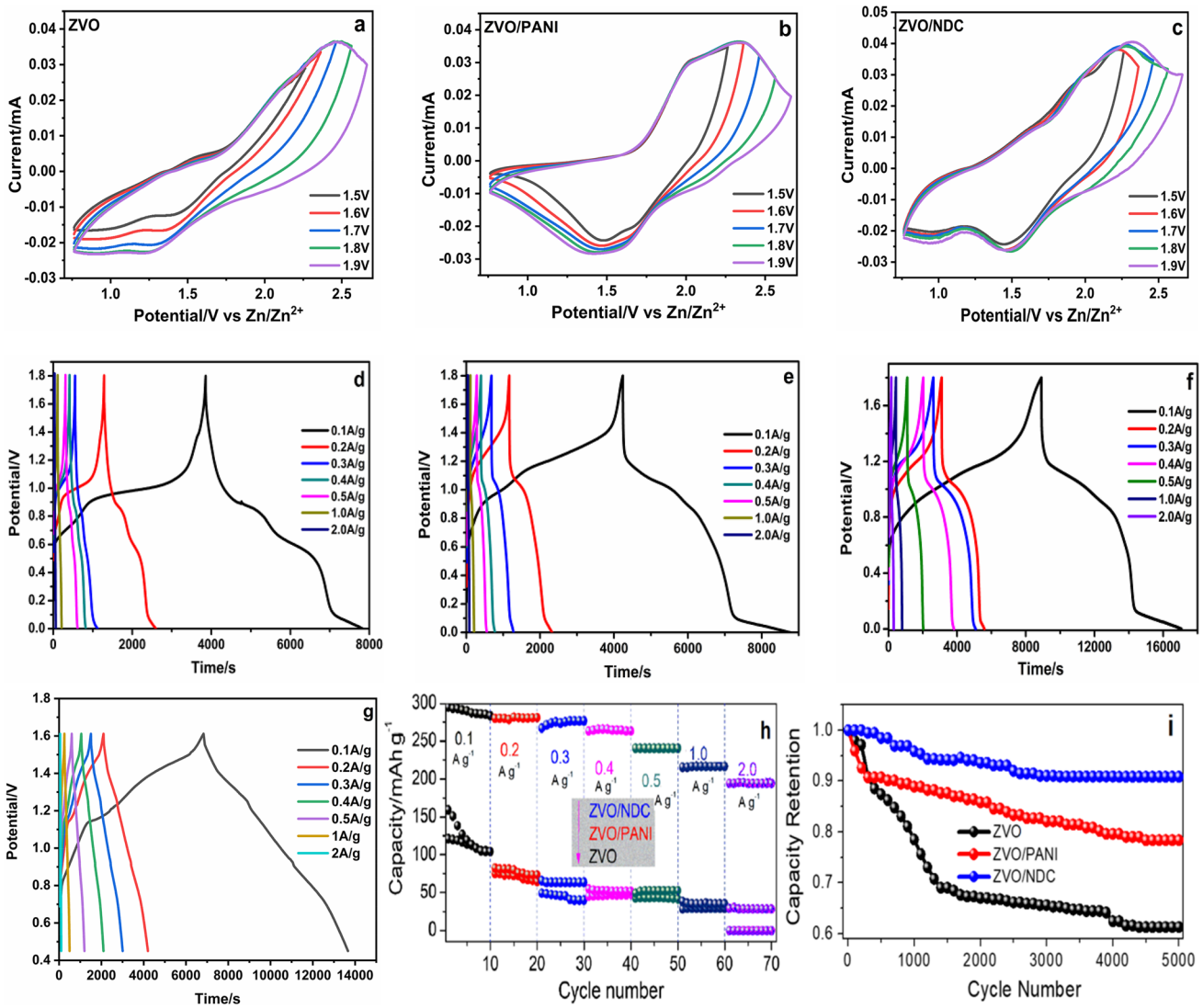

Fig. 10 CV curves of ZVO (**a**), ZVO/PANI (**b**), and ZVO/NDC (**c**) in different voltage windows; GCD curves of ZVO (**d**), ZVO/PANI (**e**), ZVO/NDC (**f**), and NDC (**g**) at different current densities. Capacity variation at different current densities (**h**) and stability curves (**i**) of ZVO, ZVO/PANI, and ZVO/NDC

which enhances the conductivity. As a result, the ZVO/NDC used as cathode demonstrates improved capacity of 295 mAh g^{-1} at 0.1 A g^{-1} and a high-rate capability, because of the improved electron transportation of ZVO doped by NDC. In addition, ZVO/NDC also shows an impressively stack mass energy density of 132.8 mWh kg^{-1} and volumetric energy density of 39.84 mWh L^{-1}. Moreover, the capacity retention of the ZVO/NDC after 5000 cycles at 1 A g^{-1} current density is 91%, which is significantly higher than that of ZVO (61%) and ZVO/PANI (78%). The band structure feature of ZVO/NDC is simulated on the basis of density functional theory (DFT). From the experimental results and the first-principles, the structural stability and electrical conductivity of ZVO are found to be both enhanced after doped by NDC. This work highlights the proof-of-concept of designing nitrogen-rich carbon-doped electrodes for use in ZIBs.

Supplementary Information The online version contains supplementary material available at https://doi.org/10.1007/s11581-021-04312-6.

Author contribution Feifei Wang: data curation, formal analysis, methodology, validation, writing—original draft. Qiguan Wang: conceptualization, supervision, visualization, writing—review and editing. Shibo Dong: formal analysis, software. Sumin Wang: conceptualization, funding acquisition, project administration, resources, writing—review and editing.

Funding Authors acknowledged the financial support from the National Natural Science Foundation of China (Grant No. 21772152) and the Key Research and Development Program of Shaanxi (Program No. 2021GY-220).

Declarations

Conflict of interest The authors declare no competing interests.

References

1. Dunn B, Kamath H, Tarascon JM (2011) Electrical energy storage for the grid: a battery of choices. Science 334(6058):928–993
2. Armand M, Tarascon JM (2008) Building better batteries. Nature 451:652–657
3. Tarascon JM, Armand M (2001) Issues and challenges facing rechargeable lithium batteries. Nature 414:359–367
4. Zuo W, Zhu W, Zhao D, Sun Y, Li Y, Liu J, Lou XW (2016) Bismuth oxide: a versatile high-capacity electrode material for rechargeable aqueous metal-ion batteries. Energy Environ Sci 9:2881–2891
5. Pasta M, Wessells CD, Huggins RA, Cui Y (2012) A high-rate and long cycle life aqueous electrolyte battery for grid-scale energy storage. Nat Commun 3:1149
6. Yan J, Wang J, Liu H, Bakenov Z, Gosselink D, Chen P (2012) Rechargeable hybrid aqueous batteries. J Power Sources 216:222–226
7. Ming FW, Liang HF, Lei YJ, Kandambeth S, Eddaoudi M, Alshareef HN (2018) Layered $Mg_xV_2O_5•nH_2O$ as cathode material for high performance aqueous zinc ion batteries. ACS Energy Lett 3:2602–2609
8. Kundu D, Adams BD, Duffort V, Vajargah SH, Nazar LF (2016) A high-capacity and long-life aqueous rechargeable zinc battery using a metal oxide intercalation cathode. Nat Energy 1:16119
9. He P, Yan M, Zhang G, Sun R, Chen L, An Q, Mai L (2017) Layered VS_2 nanosheet-based aqueous Zn ion battery cathode. Adv Energy Mater 7:1601920
10. Lee J, Ju JB, Cho WI, Cho BW, Oh SH (2013) Todorokite-type MnO_2 as a zinc-ion intercalating material. Electrochim Acta 112:138–143
11. Xu C, Li B, Du H, Kang F (2012) Energetic zinc ion chemistry: the rechargeable zinc ion battery. Angew Chem Int Ed 51:933–935
12. Trocoli R, Mantia FLa, (2015) An aqueous zinc-ion battery based on copper hexacyanoferrate. Chemsuschem 8:481–485
13. Li G, Yang Z, Jiang Y, Jin C, Huang W, Ding X, Huang Y (2016) Towards polyvalent ion batteries: a zinc-ion battery based on NASICON structured $Na_3V_2(PO_4)_3$. Nano Energy 25:211–217
14. Xia C, Guo J, Lei Y, Liang H, Zhao C, Alshareef HN (2018) Rechargeable aqueous zinc-Ion battery based on porous framework zinc pyrovanadate intercalation cathode. Adv Mater 30:1705580
15. Yang YQ, Tang Y, Fang GZ, Wang LB, Zhou J, Liang SQ (2018) Li^+ intercalated $V_2O_5·nH_2O$ with enlarged layer spacing and fast ion diffusion as an aqueous zinc-ion battery cathode. Energy Environ Sci 11:3157–3162
16. Xia C, Guo J, Li P, Zhang X, Alshareef HN (2018) Highly stable aqueous zinc-ion storage using a layered calcium vanadium oxide bronze cathode. Angew Chem Int Ed 57:3943–3948
17. Ding JW, Du ZG, Gu LQ, Li B, Gong YJ, Yang SB (2018) Ultrafast Zn^{2+} intercalation and deintercalation in vanadium dioxide. Adv Mater 30:1800762
18. Wan F, Zhang LL, Dai X, Wang XY, Niu ZQ, Chen J (2018) Aqueous rechargeable zinc/sodium vanadate batteries with enhanced performance from simultaneous insertion of dual carriers. Nat Commun 9:1656
19. He B, Zhou Z, Man P, Zhang Q, Li C, Xie L, Wang X, Li Q, Yao YG (2019) V_2O_5 nanosheets supported on 3D n-doped carbon nanowall arrays as an advanced cathode for high energy and high power fiber-shaped zinc-ion batteries. J Mater Chem A 7:12979–12986
20. Li Q, Zhang Q, Liu L, Zhou Z, Li C, He B, Man P, Wang X, Yao YG (2019) Anchoring V_2O_5 nanosheets on hierarchical titanium nitride nanowire arrays to form core-shell heterostructures as a superior cathode for high-performance wearable aqueous rechargeable zinc-ion batteries. J Mater Chem A 7:12997–13006
21. Chao DL, Zhu CR, Song M, Zhao HF, Wang J, Wang RM, Zhang H, Fan HJ (2018) A high-rate and stable quasi-solid-state zinc-ion battery with novel 2D layered zinc orthovanadate array. Adv Mater 30:1803181
22. Xu D, Wang H, Li F, Wang GZ, R, He B, Gong Y, Hu X, (2019) Conformal conducting polymer shells on V_2O_5 nanosheet arrays as a high-rate and stable zinc-ion battery cathode. Adv Mater Interfaces 6:1801506
23. Gupta SK, Ghosh PS, Yadav AK, Jha SN, Bhattacharyya D, Kadam RM (2017) Origin of blue-green emission in alpha-$Zn_2P_2O_7$ and local structure of Ln(3+) ion in alpha-$Zn_2P_2O_7$:Ln(3+) (Ln=Sm, Eu): time-resolved photoluminescence, EXAFS, and DFT measurements. Inorg Chem 56:167–178
24. Zhang K, Wang Q, Thota A, Zhang W, Chen J, Wang Y, Wu X, Wang S (2020) Flexible 3D hierarchical porous $NiCo_2O_4$/CC electrode decorated by nitrogen-doped carbon from polyaniline carbonization for high-performance supercapacitors. J Mater Sci 55:5982–5993
25. Guo J, Ming J, Lei Y, Zhang W, Xia C, Cui Y, Alshareef HN (2019) Artificial solid electrolyte interphase for suppressing surface reactions and cathode dissolution in aqueous zinc ion batteries. ACS Energy Lett 4:2776–2781
26. Wang Q, Wang S, Li J, Moriyama H (2012) Synthesis and characterization of C60/polyaniline composites from interfacial polymerization. J Polym Sci Part B: Polym Phys 50:1426–1432
27. Wang M, Shi Y, Jiang G (2012) 3D hierarchical $Zn_3(OH)_2V_2O_7·2H_2O$ and $Zn_3(VO_4)_2$ microspheres: synthesis, characterization and photoluminescence. Mater Res Bull 47:18–23
28. Ding W, Wei Z, Chen S, Qi X, Yang T, Hu J, Wang D, Wan LJ, Alvi SF, Li L (2013) Space-confinement-induced synthesis of pyridinic-and pyrrolic-nitrogen-doped graphene for the catalysis of oxygen reduction. Angew Chem Int Ed 52:11755–11759
29. Kim YS, Tai WP, Shu SJ (2005) Effect of preheating temperature on structural and optical properties of ZnO thin films by sol-gel process. Thin Solid Films 491(1/2):153–160
30. Jiang H-Q, Endo H, Natori H, Nagai M, Kobayashi K (2009) Fabrication and efficient photocatalytic degradation of methylene blue over CuO/$BiVO_4$ composite under visible-light irradiation. Mater Res Bull 4:700–706
31. Pan Z, Yang J, Yang J, Zhang Q, Zhang H, Li X, Kou Z, Zhang Y, Chen H, Yan C, Wang J (2020) Stitching of $Zn_3(OH)_2V_2O_7·2H_2O$ 2D nanosheets by 1D carbon nanotubes boosts ultrahigh rate for wearable quasi-solid-state zinc-ion batteries. ACS Nano 14:842–853
32. Sarkar A, Sarkar S, Sarkar T, Kumar P, Bharadwaj MD, Mitra S (2015) Rechargeable sodium-ion battery: high-capacity ammonium vanadate cathode with enhanced stability at high rate. ACS Appl Mater Inter 7:17044–17053
33. Reed LD, Menke E (2013) The roles of V_2O_5 and stainless steel in rechargeable Al-ion batteries. J Electrochem Soc 160:A915–A917

34. Miao X, Chen Z, Wang N, Nuli Y, Wang J, Yang J, Hirano S (2017) Electrospun V_2MoO_8 as a cathode material for rechargeable batteries with Mg metal anode. Nano Energy 34:26–35
35. Ma W, Ma R, Wang C, Liang J, Liu X, Zhou K, Sasaki T (2015) A superlattice of alternately stacked Ni-Fe hydroxide nanosheets and graphene for efficient splitting of water. ACS Nano 9:1977–2198
36. Song F, Hu X (2014) Ultrathin cobalt-manganese layered double hydroxide is an efficient oxygen evolution catalyst. J Am Chem Soc 136:16481–16484
37. Balasubramanian MM, Subramani M, Murugan D, Ponnusamy S (2020) Groundnut shell-derived porous carbon-based supercapacitor with high areal mass loading using carbon cloth as current collector. Ionics 26:6297–6308